remote sensing

MDPI

Article

Estimation of PMx Concentrations from Landsat 8 OLI Images Based on a Multilayer Perceptron Neural Network

Bo Zhang [1,2], Meng Zhang [1,*], Jian Kang [3], Danfeng Hong [2,3], Jian Xu [2] and Xiaoxiang Zhu [2,3]

[1] School of Human Settlements and Civil Engineering, Xi'An Jiaotong University, Xi'an 710049, China; zhangbo5005@stu.xjtu.edu.cn
[2] Remote Sensing Technology Institute (IMF), German Aerospace Center (DLR), 82234 Wessling, Germany; danfeng.hong@dlr.de (D.H.); jian.xu@dlr.de (J.X.); xiaoxiang.zhu@dlr.de (X.Z.)
[3] Signal Processing in Earth Observation (SiPEO), Technical University of Munich (TUM), 80333 Munich, Germany; jian.kang@tum.de
* Correspondence: sql_zhang@hotmail.com; Tel.: +86-186-2903-4600

Received: 16 February 2019; Accepted: 11 March 2019; Published: 16 March 2019

Abstract: The estimation of PM_x (incl. PM_{10} and $PM_{2.5}$) concentrations using satellite observations is of great significance for detecting environmental issues in many urban areas of north China. Recently, aerosol optical depth (AOD) data have been being used to estimate the PM_x concentrations by implementing linear and/or nonlinear regression analysis methods. However, a lot of relevant research based on AOD published so far have demonstrated some limitations in estimating the spatial distribution of PM_x concentrations with respect to estimation accuracy and spatial resolution. In this research, the Google Earth Engine (GEE) platform is employed to obtain the band reflectance (BR) data of a large number of Landsat 8 Operational Land Imager (OLI) remote sensing images. Combined with the meteorological, time parameter and the latitude and longitude zone (LLZ) method proposed in this article, a new BR (band reflectance)-PM_x (incl. PM_{10} and $PM_{2.5}$) model based on a multilayer perceptron neural network is constructed for the estimation of PM_x concentrations directly from Landsat 8 OLI remote sensing images. This research used Beijing, China as the test area and the conducted experiments demonstrated that the BR-PM_x model achieved satisfactory performances for the PM_x-concentration estimations. The coefficient of determination (R^2) of the BR-$PM_{2.5}$ and BR-PM_{10} models reached 0.795 and 0.773, respectively, and the root mean square error (RMSE) reached 20.09 $\mu g/m^3$ and 31.27 $\mu g/m^3$. Meanwhile, the estimation results have been compared with the results calculated by Kriging interpolation at the same time point, and the spatial distribution is consistent. Therefore, it can be concluded that the proposed BR-PM_x model provides a new promising method for acquiring accurate PM_x concentrations for various cities of China.

Keywords: multilayer perceptron; neural network; Landsat 8 OLI; remote sensing image; estimation; PM_x concentrations

1. Introduction

With the rapid development of the economy in China, the processes of industrialization and urbanization have increased the environmental burden, and air pollution has become increasingly serious. Aerosols, which not only have an impact on global climate change but also on the environmental quality of the atmosphere and human health, have become the primary pollutant affecting ambient air quality in most parts of China. Simultaneously, it has been shown that increasing the concentration of aerosol particles is an important reason for the frequent "haze" weather in cities and suburban areas [1–3]. Therefore, the estimation of aerosol PM_x (including PM_{10} and $PM_{2.5}$) has become a popular research topic in recent years [4–7]. Aerosols have the characteristics of continuous occurrence and large spatial variability in concentration. Due to the uneven distribution of ground monitoring stations, it is difficult to obtain the accurate distributions of aerosol data together with their change trends for an entire city by the methods of spatial interpolation and/or numerical simulation based on the data from monitoring stations [8,9]. Taking advantages of high timeliness, wide coverage and high resolution, the technique of satellite remote sensing makes it possible to monitor the aerosol conditions on a larger spatial scale [10–12].

Research on PM_x estimation based on satellite remote sensing images began in the 1990s [13]. With the rapid improvement of sensor spectral detection capabilities and the appearance of imaging spectrometers, the satellite data of Moderate Resolution Imaging Spectroradiometer (MODIS) [14], Multi-angle Imaging Spectroradiometer (MISR) [15], Geostationary Meteorological Satellite-5 (GMS-5) [16], Huanjing-1(HJ-1) [17], Himawari-8 [18] and Landsat 8 Operational Land Imager (OLI) have been used for aerosol retrieval studies in the past decades [19].

Meanwhile, a number of previous studies have been conducted to investigate the quantitative relationships between AOD (aerosol optical depth) and PM_x concentrations [20–22]. The AOD-PM_x model is constructed by linear or nonlinear regression, which can be employed to accurately estimate ground-level particulate matter, partly by accounting for relative humidity (RH), wind speed (WS), temperature (TEMP) and planetary boundary layer height (PBLH) [23–25]. More recently, Artificial Neural Networks (ANNs) have proven to be an advanced mathematical model to achieve better regression results compared with simple linear/nonlinear regression analysis [26,27].

Although some AOD-PM_x models can be used to estimate PM_x well in some areas, it is still essential to evaluate the robustness of these methods. Paciorek and Liu [28]. highlighted the limitations of AOD in predicting the spatial distribution of $PM_{2.5}$; Kumar [29] summarized some of the factors that affect the AOD-$PM_{2.5}$ association, such as mismatch in spatial-temporal resolution, decomposition of AOD by aerosol types, collocation of AOD and $PM_{2.5}$ data, and control for spatial–temporal structure in the statistical model. In view of the relative weaknesses between AOD and $PM_{2.5}$ in the study of Paciorek and Liu [28], some of the findings need further analysis.

This research is dedicated to developing a so-called BR (band reflectance)-PM_x model based on the algorithm of a multilayer perceptron neural network for the estimation of the PM_x (including PM_{10} and $PM_{2.5}$) concentrations, where the various meteorological factors and the time parameter are jointly considered. As a result, the PM_x-concentration estimations with high spatial resolution and complete spatial coverage have been realized.

2. Materials and Methods

According to several previous research works concerning the aerosol retrievals from satellite remote sensing images [19,30], the band 1 (0.43–0.45 μm), band 3 (0.53–0.59 μm) and band 7 (2.11–2.29 μm) of Landsat 8 OLI have been considered to be relevant to PM_x concentrations. Considering that the band reflectance can be affected by the land surface reflectance, normalized difference vegetation index (NDVI) has been also employed in the proposed BR-Model to realize a more reasonable evaluation of the atmospheric contribution to this reflectance. In this research, the Google Earth Engine (GEE) cloud computing platform has been employed to obtain a large number of consecutive historical satellite image data (Landsat 8 OLI) over the whole area of China from May 2014 to May 2018. Meanwhile, (a) the hourly PM_x concentration extracted from the China Environmental Monitoring Center (CEMC) and (b) the meteorological parameters, such as relative humidity (RH), temperature (TEMP), wind direction (WD), wind speed (WS) and atmospheric pressure (PRS) have also been implemented in this research. It should be mentioned that the data of (b) (viz. the meteorological parameters) were initially captured by China Meteorological Administration and had been sent to the National Centers for Environmental Information of National Oceanic and Atmospheric Administration (NOAA) U.S. Department of Commerce for further disseminations. In order to facilitate the description, these meteorological parameters will be termed as 'NOAA data' in the following paragraphs of this article. Moreover, a new method has been developed to explore the 'optimal' latitude and longitude range of the subset for ANN trainings. This method is termed as an LLZ (latitude and longitude zone) method and can be employed by the proposed BR-PM_x model to enhance the estimation precision of the PM_x concentrations in different research areas.

2.1. Data Collection and Preprocessing

As illustrated in Table 1, three types of data are employed in this research: (a) Landsat 8 OLI remote sensing images from the Google Earth Engine (GEE) platform, (b) hourly PM_x concentrations from the China Environmental Monitoring Station (CEMS) and (c) meteorological parameters of RH, PRS, TEMP, WD and WS from the National Oceanic and Atmospheric Administration (NOAA).

Table 1. Details of all datasets used in this study.

Category	**Variables**	**Unit**	**Temporal Resolution**	**Source**
PM_x concentration	$PM_{2.5}$ PM_{10}	μg/m^3	1 h	China Environmental Monitoring Center (CEMC)
Satellite image data of Landsat 8 Operational Land Imager (OLI)	Band1 Band3 Band7 NDVI	Band Reflectance	16 day	Google Earth Engine (GEE)
Meteorological parameters	RH	%	3 h	National Oceanic and Atmospheric Administration (NOAA)
	PRS	Pa	3 h	
	TEMP	K	3 h	
	WD	°	3 h	
	WS	m/s	3 h	

2.1.1. Landsat 8 OLI Data

The Landsat 8 satellite, which carries the Operational Land Imager (OLI) and the Thermal Infrared Sensor (TIRS), was successfully launched by NASA on 11 February 2013. The OLI covers all nine bands of the ETM+ sensor. Due to the generic nature of higher resolution and wider band coverage, the Landsat 8 data have been widely used in Earth resource exploration, natural disaster, agriculture, forestry, animal husbandry management and environmental pollution monitoring.

The Google Earth Engine (GEE) cloud computing platform is a facility for processing remote sensing images in bulk under Google Inc. in Mountain View, CA, USA. As one of the most advanced platforms for the analysis and visualization of geographical data, GEE is able to provide users with a large amount of historical satellite image data for consecutive years (e.g., the MODIS, Landsat, etc.). Meanwhile, GEE also provides algorithms and tools for processing and analyzing petabyte data for information mining [31–33]. As one significant subset of Landsat 8 OLI/TIRS data, the " USGS Landsat 8 Collection 1 Tier 1" has been employed as the primary data for the estimation of PM_x concentrations in this study considering that (a) the data in this subset can accurately calibrate the top-of-atmosphere (TOA) reflectance and (b) its temporal resolution is 16 days in China, which is shorter than some other subsets of Landsat 8 OLI/TIRS. Then, a JavaScript program was developed in GEE to obtain, adjust and correct the data from thousands of Landsat 8 OLI images by the method of orthorectification and geographical registration. After that, the selected images are processed using the following steps: (a) remove cloud by the function of mask algorithm (FMask) provided by GEE, (b) establish a circular buffer around each CEMC monitoring station, where the radius of the buffer is 15 meters, viz. the half resolution of Landsat 8 OLI data (30 m), (c) extract the band reflectance of bands 1, 3 and 7 from

Landsat 8 OLI images of all the pixels falling inside each established buffer, (d) calculate NDVI from band 4 and band 5 of the Landsat 8 OLI data and (e) calculate the average values of the band reflectance and NDVI in each established buffer. After the data processing from step (a) to (e), the calculated average values together with the imaging time properties were assigned to their corresponding CEMC monitoring stations, which can be regarded as the primary source data for the proposed BR-PM_x models. It should be mentioned that the imaging time property will be used as temporal reference in the following processes.

2.1.2. PMx Concentration Data of the China Environmental Monitoring Center (CEMC)

Hourly PM_x data can be collected from the China urban air quality real-time release platform (http://106.37.208.233:20035/) maintained by the China Environmental Monitoring Center (CEMC). As one of the public institutions under the Ministry of Ecological Environment, CEMC undertakes the primary tasks of national environmental monitoring. The widespread monitoring stations enable continuous aerosol measurements by using the methods of DUSTTRAK DRX and TEOM [34], which sample ambient air hourly and provide simultaneous measurements of $PM_{2.5}$ and PM_{10}.

Considering the reliability of data quality [35], the research time interval is set from 1 May 2014 to 1 May 2018. As depicted in Figure 1, there are 1497 CEMC monitoring stations in total distributed within the study area. A time buffer interval of ±0.5 h was used to match the dataset of CEMC ground observations with the Landsat 8 OLI satellite transit phase. Thus, the data of 99,404 PM_x observations were compiled.

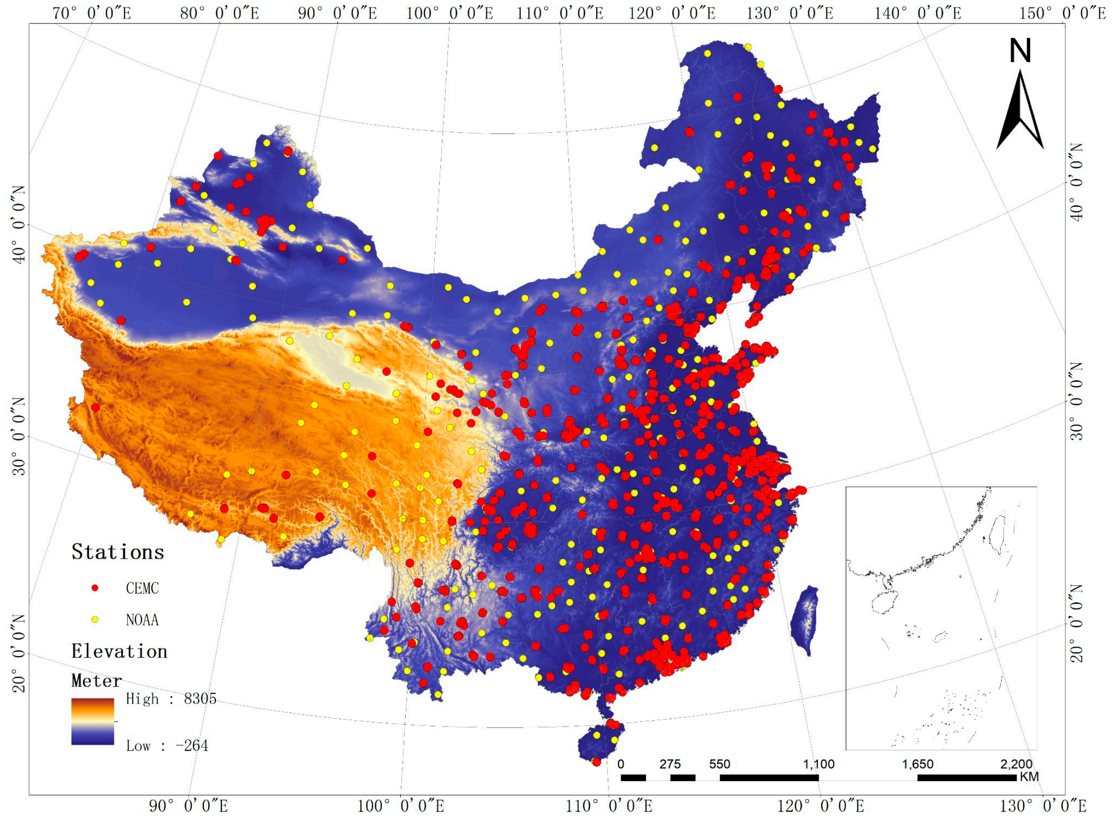

Figure 1. Research area and the spatial distribution of CEMC (red points) and NOAA (yellow points) stations used in this study.

2.1.3. Other Influence Parameters

PM_x concentration has been demonstrated to be affected by pollutant emission and meteorological situations, which exhibit significant time-varying characteristics [36]. Pollution source parameters are not discussed due to the limitations of the data source. In this study, two types of parameters were involved: the meteorological data and time data. According to the imaging time property, the Landsat 8 OLI data is assigned a 'month number (1, 2, . . . , 12)'. The 'month number' will be regarded as a time parameter in the BR-PM_x models, allowing seasonal influences to be taken into account. The meteorological data are primarily archived from the National Center for Environmental Information of NOAA, which involve qualified daily, monthly, seasonal, and yearly measurements of temperature, wind, precipitation, etc. The daily measurement produces data every 3 h starting at 0:00 UTC (viz.8:00 am Beijing time), of which the nearest neighbor time method was used for data selection. The meteorological variables selected in the proposed BR-PM_x model are RH, TEMP, WD, WS, and atmospheric pressure (PRS). Over the study area (ref. Figure 1), there are 372 NOAA stations with 949,531 meteorological observations during the period.

In the process of geospatial analysis, it is essential to ensure that all of the relevant elements are at the same or very approximate temporal stamps. The imaging time property of the Landsat 8 OLI data is regarded as the temporal reference for the conducted research. Due to the different time periods of the CEMC and NOAA measurements, the time buffer intervals of ±0.5 h and ±1 h are settled for data from CEMC and NOAA, respectively, to obtain the required parameter datasets. In this way, the data from Landsat 8 OLI, CEMC and NOAA can be harmonized together.

2.2. Methodology

Figure 2 shows the workflow used to estimate the PM_x concentrations, which requires four groups of source data, viz. (a) the 'time parameter' extracted from Landsat 8 OLI, (b) the preprocessed Band 1, 3, 7 and NDVI from Landsat 8 OLI, (c) meteorological parameters (viz. RH, PRS, TEMP, WD, WS) at NOAA stations, and (d) PM_x ($PM_{2.5}$ and PM_{10}) monitoring values at CEMC stations.

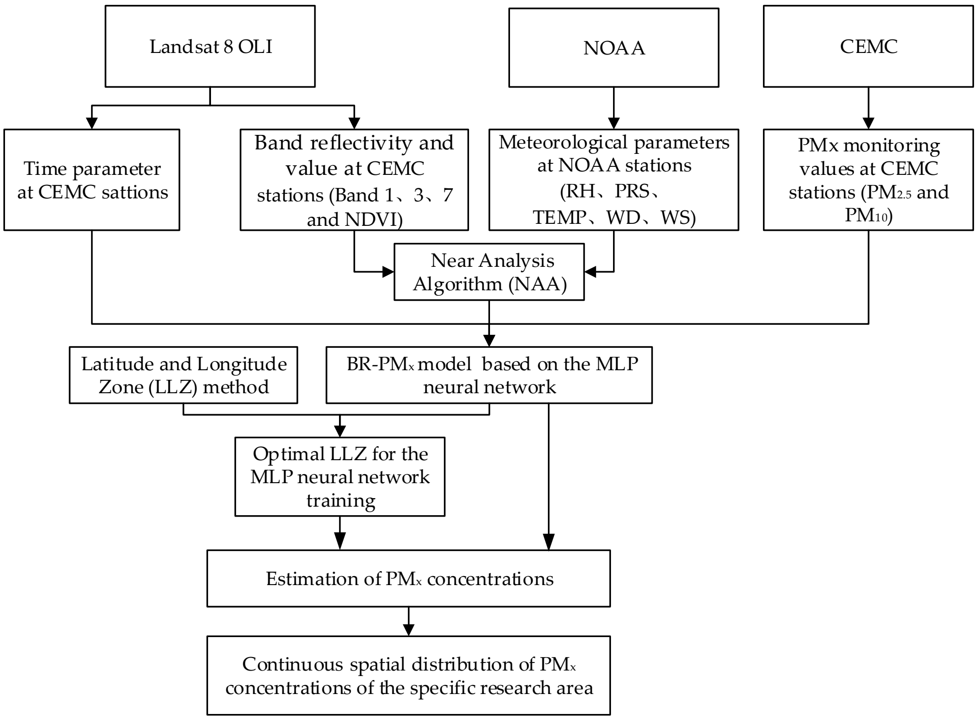

Figure 2. The workflow of PM_x concentration estimations.

Before inputting to the proposed BR-PM_x model, the data of (b) and (c) need to be integrated together by the Near Analysis Algorithm (NAA) (Section 2.2.1, below). The estimation of the PM_x concentrations are primarily based on multilayer perceptron (MLP) neural network (Section 2.2.2, below). In order to enhance the estimation accuracy for the PM_x concentrations in an entire city, the latitude and longitude zone method (Section 2.2.3, below) has been developed as well as employed by the proposed BR-PM_x model, which can help to settle the 'optimal' region of the 'MLP neural network training' for the specific research area.

2.2.1. Near Analysis Algorithm (NAA)

Due to the different number of monitoring stations and geographic locations, it is complex to directly obtain the meteorological information around the CEMC stations. Therefore, the collocation of various meteorological parameters of the investigated CEMC stations has become a priority condition for PM_x estimation.

To integrate the CEMC observations and NOAA datasets into the processes of estimating PM_x concentrations seamlessly, the NAA has been employed to compute the distance from each feature in the analytic objects (viz. the 'Input Elements' of CEMC) to the nearest features in the neighboring objects (viz. the 'Proximity Elements' of NOAA), within the settled search radius (e.g., 100 km). Thus, the nearest dataset of the monitoring stations can be calculated. Then, the necessary meteorological variables around one CEMC station can be acquired from its nearest NOAA station.

2.2.2. Multilayer Perceptron (MLP) Neural Network

Physical models are considered to be the most suitable predictors of small-scale PM_x concentrations. However, the complexity of physical models and some other influential factors make it hard to achieve the macroscopic estimation of PM_x. Statistical regression and ANN approaches are considered a promising method for estimating PM_x concentrations.

A neural network is an important technology for pattern recognition and machine learning. It is the basis of deep learning that simulates the neural network of the human brain to realize artificial intelligence. It has been widely used for diverse remote sensing applications [37,38]. The neural network consists of many interconnected processing units. These units are usually linearly arranged into groups, which can be simulated by electronic circuits or computer programs. Multilayer perceptron (MLP) is a forward-structured ANN, where the input vectors are mapped to output vectors, and the representative models involve a multilayer BPN network [39], RBF network [40], the Hopfield model [41] and so on.

In this paper, the BPN (back-propagation network) is selected for PM_x concentration estimation. BPN is a multilayered network for weights' training with forward nonlinear differentiable functions. The BPN neural network consists of input layer, multiple hidden layers and the output layer (see Figure 2). Each of these layers is connected to all of the cells in the adjacent layer. Simultaneously, there is no connection between the cells of the same layer. Once a pair of learning samples is provided to the network, the activation value of the neuron propagates from the input layer to the output layer, and the neurons in the output layer obtain the input response of the network. After that, the connection weights are modified layer by layer from the output layer through the middle layer and then back to the input layer.

In Figure 3, X_i is the input of node i of the input layer, $i = 1 \ldots N$, W_{ij} is the weight between node j of the hidden layer and the node i of the input layer, $j = 1 \ldots p$, θ_j is the threshold of the node j of the hidden layer; θ_k is the threshold of the node k of the hidden layer; $\phi(X)$ is the excitation function of the hidden layer; W_{jk} is the weight between node k of the hidden layer and node j of the hidden layer, $k = 1 \ldots q$. W_{kl} is the weight between node l of the output layer and node k of the hidden layer, $l = 1 \ldots M$. O_l represents the threshold of node l of the output layer, $l = 1 \ldots M$, $\varphi(X)$ is the excitation function of the output layer, and $Y(PM_X)$ is the output layer node.

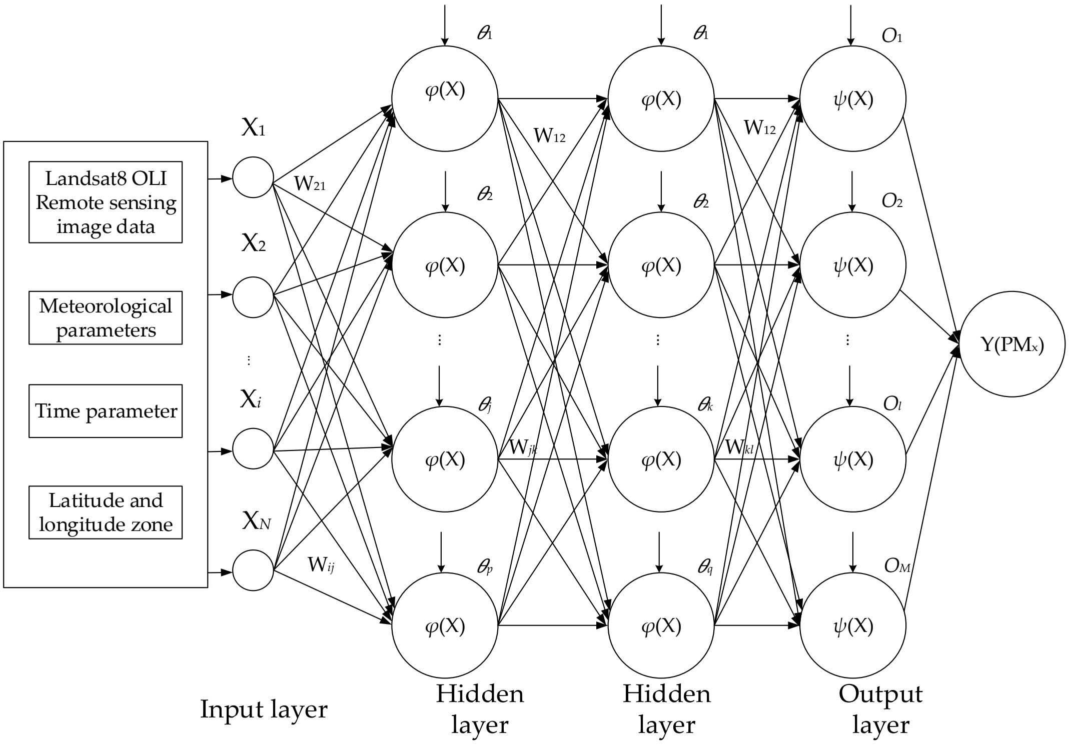

Figure 3. The diagram of the back-propagation network (BPN).

In this research, a 4-layer BPN neural network has been developed to estimate the PM_x concentration. In the process of determining the input and output factors of the model, (a) the band reflectance of band 1, 3, 7 and the band value of NDVI at the CEMC monitoring stations from the Landsat 8 OLI images are considered as the 'band parameter'; (b) the NAA method has been utilized to obtain the meteorological data (viz. RH, PRS, TEMP, WD and WS) around the CEMC stations based on the NOAA data; and (c) the dataset of 'actual' values of PM_x concentration have been measured by CEMC stations. In addition, the latitude and longitude zone (LLZ) method has been developed to get the optimal training region (Section 2.2.3, below). The input variables of the proposed BPN model refer to the 'band parameter', the meteorological data and the corresponding time parameter, while the output variables are the measured PM_x concentrations at CEMC stations. To improve the computational speed and PM_x concentration estimation accuracy, the input and output data must be normalized uniformly to the data range of $[-1,1]$.

For the topologic design of the neural network, the tansig function (tan-sigmoid transfer function, see Figure 4a) is utilized for transmitting the neurons of each layer [42]. The purelin function (linear transfer function, see Figure 4b) is employed as the transfer function of the output layer [43,44]. The number of intermediate nodes of the hidden layers is enlarged from 5 to 20 in a stepwise fashion using the Kolmogorov theorem to establish the nodes of the network structure [45]. Based on the growth method of the network structure, the best number of nodes of the hidden layers is selected as (15, 15) for the continuous training of the network.

In the process of neural network operation, the input data are randomly divided into three subsets. The first subset is for training (60%), the second is for validation (20%), and the third is for testing (20%). The data in the training subset are used to train and adjust the weights on the four-layer neural networks. The validation subset is required to minimize overfitting. The data in the testing subset are implemented to predict the PM_x concentration data by the BPN model, for which the optimal connection weights should be determined during the training process. The performance of the established neural network model can be primarily evaluated according to the factors of root mean square error (RMSE) and coefficient of determination (R^2) between the predicted and the observed value.

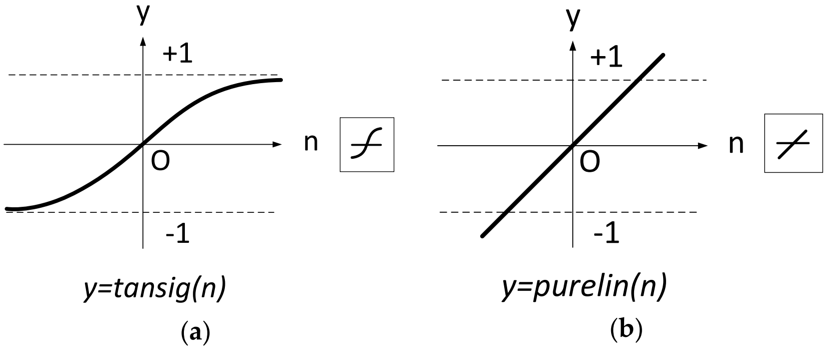

Figure 4. Transfer functions utilized in the BPN: (**a**) the tansig function and (**b**) the purelin function.

2.2.3. Latitude and Longitude Zone (LLZ) Method

As mentioned earlier, the Latitude and Longitude Zone (LLZ) method can be implemented to compute the 'optimal' training region for one specific research area (viz. one city), which can be characterized by six steps:

(a) the geometric center of the research area is settled as the center point of the latitude and longitude zone (LLZ);

(b) the initial latitude and longitude width can be calculated by Equation (1):

$$(Lon_{width}, Lat_{width}) = \xi(Lon_{area}, Lat_{area}) \quad (1)$$

where Lon_{width} and Lat_{width} respectively represent the longitude and latitude width of the initial LLZ, Lon_{area} and Lat_{area} represent the longitude and latitude widths of the minimum enclosing rectangle (MER) of the research area; and ξ is a coefficient that can be empirically settled between 0.5 and 1.

(c) the LLZ is progressively growing at 0.1 degrees along both of the longitude and latitude directions;

(d) the monitoring datasets falling inside the LLZ are selected and inputted to the proposed BR-PM_x models for the MLP Neural Network training;

(e) The eigenvalue R^2 will be calculated after the MLP Neural Network training, which can reflect the current accuracy of the PM_x concentration estimation;

(f) the steps (c) to (e) will be continuously operated until the area of LLZ becomes K times larger than the MER of the specific research area, where K can be empirically settled as 2, 3, ... N.

(g) the R^2 of all of the LLZs will be compared to each other, and then the LLZ with the largest R^2 will be picked out as the 'optimal' training region of the specific research area.

As illustrated by Figure 5, the 'optimal' training region of LLZ is relevant to distribution of the monitoring stations, which could be smaller, larger or quite similar to the MER of the research area. It is worth mentioning that it is not desired if the LLZ is much smaller than the MER of the research area. Such undesired conditions could be avoided by the empirical coefficient ξ settled in step (b).

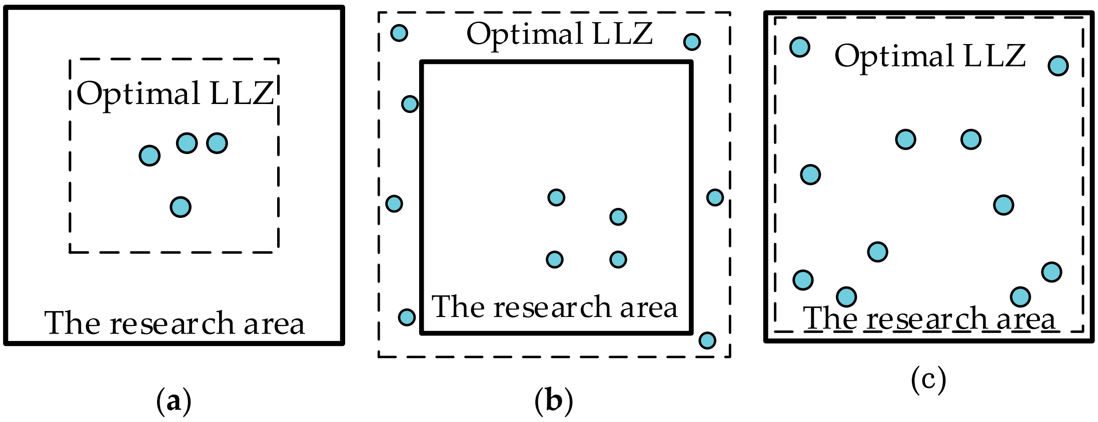

Figure 5. The diagrammatic sketch of the 'optimal' LLZ which could be (**a**) smaller, (**b**) larger or (**c**) quite similar to the MER of the specific research area; rectangle with solid line: MER of the research area; rectangle with dashed line: optimal LLZ; blue dots: the monitoring stations.

3. Results

3.1. PMx Estimations Based on MLP Neraul Network in the Whole Area of Mainland China

Based on the MLP neural network, the PM_x concentrations have been estimated in the whole area of mainland China. Several previous studies have demonstrated the temporal patterns of PM_x concentrations, i.e., the PM_x concentrations may vary with months and/or seasons [46,47]. Hence, the R^2 between PM_{est} and PM_{rea} is calculated for different months (from January to December) and seasons (from spring to winter). Then, the scatter plots of PM_{est} and PM_{rea} are drawn from the 70,393 samples for the BR-$PM_{2.5}$ model and 67,265 samples for the BR-PM_{10} model by the line regression functions provided by MATLAB 2016, MathWorks Inc, Natick, USA (see Figure 6). With the BR-$PM_{2.5}$ model, the R^2 is 0.3647, and the root mean square error (RMSE) is 25.34 (μg/m^3), while with the BR-PM_{10} model, the R^2 is 0.2928 and the RMSE is 36.66 (μg/m^3). Obviously, neither result is satisfactory.

To further investigate the temporal aerosol variations, the proposed BR-PM_x models are implemented to estimate the concentrations of $PM_{2.5}$ and PM_{10} in each month and season from 2014 to 2018. The relevant regression coefficients of the estimation results are illustrated in Table 2. For all monthly and seasonal regression calculations, the R^2 of the BR-$PM_{2.5}$ model is generally slightly higher than that of the BR-PM_{10} model, while the RMSE of the BR-$PM_{2.5}$ model is much smaller. For the BR-$PM_{2.5}$ model, R^2 exhibited a seasonal behavior characterized by a maximum during autumn (0.4280), lower values in spring (0.3910) and summer (0.3813), and a minimum in winter (0.3754), which roughly agrees with the findings of Engel-Cox et al. [48]. For the BR-PM_{10} model, the maximum value of R^2 also exists in autumn (0.3407), followed by winter (0.3233), summer (0.2866) and spring (0.2646).

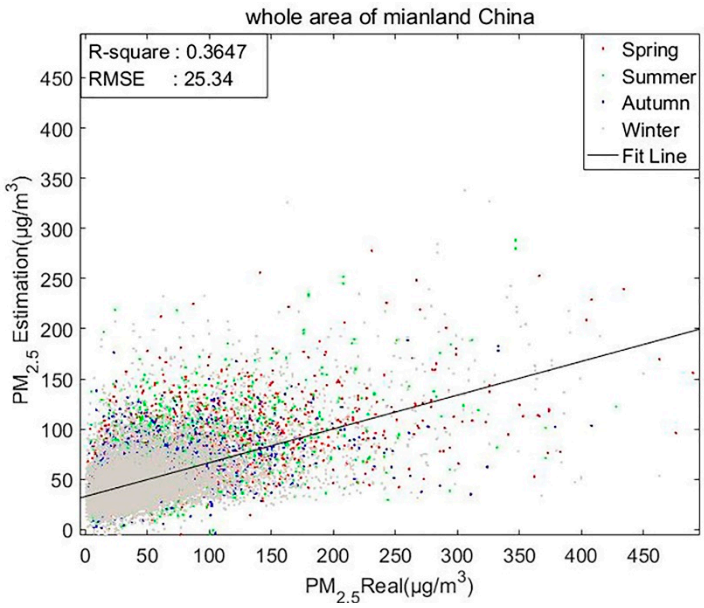

(**a**)

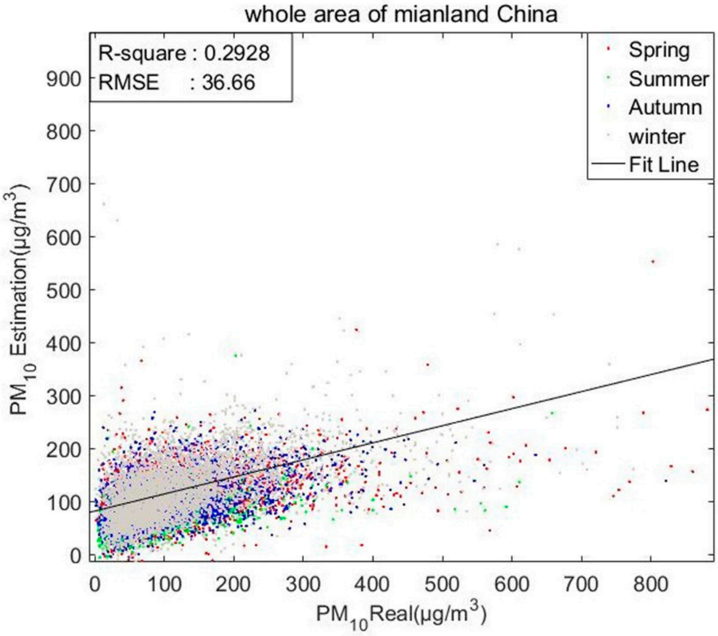

(**b**)

Figure 6. Scatterplots between PM_{est} and PM_{rea} of (**a**) the BR-$PM_{2.5}$ model and (**b**) BR-PM_{10} model in the whole area of mainland China, where the solid line represents the fit line obtained.

Table 2. Regression coefficients of BR-PM_x models using the samples in each month/season from 2014 to 2018.

Period	BR-$PM_{2.5}$			BR-PM_{10}		
	R^2	RMSE	N	R^2	RMSE	N
March	0.3141	28.35	6831	0.3186	55.83	6597
April	0.2926	23.27	5195	0.2208	39.99	5078
May	0.3588	23.57	4580	0.2606	42.45	4438
June	0.3817	20.59	5172	0.3068	37.38	4896
July	0.3405	21.06	5404	0.2613	25.77	5128
August	0.3476	21.2	5699	0.2689	31.77	5377
September	0.3112	15.35	5374	0.2928	21.23	5111
October	0.3814	28.01	6290	0.3423	39.29	6011
November	0.3482	30.38	5767	0.2829	52.67	5505
December	0.3914	40.57	6895	0.3603	47.19	6626
January	0.3877	40.6	6396	0.3805	53.16	6069
February	0.3453	30.91	6819	0.3028	49.05	6428
ALL Spring	0.3813	20.68	16606	0.2646	37.77	16113
ALL Summer	0.3910	17.28	16275	0.2866	28.34	15401
ALL Autumn	0.4280	25.4	17431	0.3407	39.77	16627
ALL Winter	0.3754	33.78	20110	0.3233	50.01	19141

3.2. Caculation of the Optimal LLZ for the Specific Research Area

To improve the accuracy of PM_x concentration estimation and reduce the values of RMSE, the LLZ method (described in Section 2.2.2) is integrated into the MLP neural network algorithm in the proposed BR-PM_x models. The capital of China, Beijing (116.39 E, 39.92 W) is selected as the test area, and the LLZ center point is set at the geometric center of Beijing, growing at 0.1 degrees along the longitude and latitude direction. Then, the monitoring datasets inside the latitude and longitude zone are continuously tested by the BR-PM_x models to explore the optimal bandwidth. Figures 7 and 8 show the variation of the coefficient of determination (R^2) between PM_{est} and PM_{rea} at different spatial ranges obtained by the LLZ method. It should be noted that the origin point of the x, y axis is (116.39, 39.92) in both Figures 7 and 8.

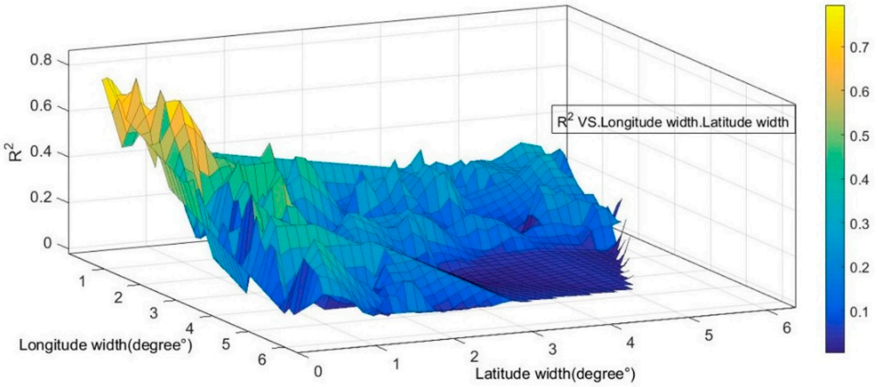

Figure 7. The coefficient of determination (R^2) between PM_{est} and PM_{rea} of the BR-$PM_{2.5}$ model at different spatial obtained by the LLZ method.

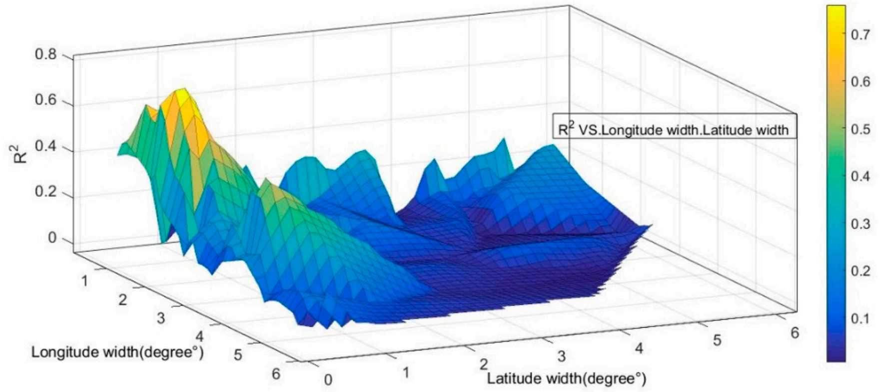

Figure 8. The coefficient of determination (R^2) between PM_{est} and PM_{rea} of the BR-PM_{10} model at different spatial ranges obtained by the LLZ method.

According to Figures 7 and 8, it is found that the variation of the R^2 between PM_{est} and PM_{rea} is not very drastic in a range with the longitude width within 2° and the latitude width within 1°. Once the latitude/longitude range is enlarged to a certain width, the R^2 values decrease dramatically. The optimal values for the coefficient R^2 of the BR-PM_X model exceed 0.7 with a longitude range of 2° and a latitude range of 1°.

Using the LLZ method, the data located inside the bandwidth of ca. 2° longitude and ca. 1° latitude with Beijing's geometric center as the center point are inputted to the BR-PM_x models. Both the BR-PM_{10} and BR-$PM_{2.5}$ models demonstrate significant improvements for the calculated estimates of the PM_x concentrations after the combination with the LLZ method. The R^2 of $PM_{2.5}$ and PM_{10} concentrations increases to 0.795 and 0.773, respectively. The RMSE is reduced by 14.6% (36.65 to 31.27) and 20.7% (25.34 to 20.09) for PM_{10} and $PM_{2.5}$, respectively (see Figure 9), which indicates that the LLZ method is very helpful for estimating the PM_x concentrations.

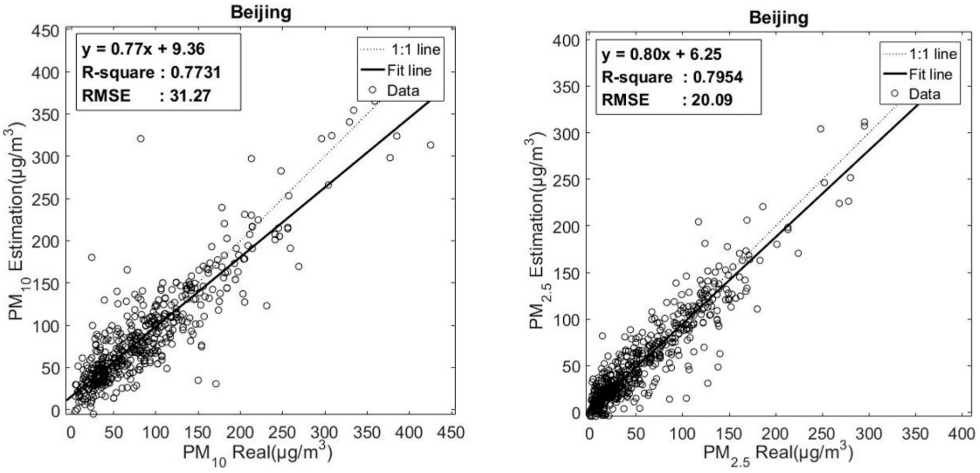

(**a**) (**b**)

Figure 9. Scatterplots between PM_{est} and PM_{rea} of (**a**) BR-PM_{10} model and (**b**) BR-$PM_{2.5}$ models combined with the LLZ method, where the solid line is the fitting line obtained by the line regression method provided by MATLAB functions and the dashed line is the reference of the linear function y = x.

3.3. Validation Analysis

As depicted in Section 2.1.1, the remote sensing images imported to the BR-PM_x model need to be processed for removing of clouds. For the mainland of China, winter is the season with the most serious air pollution, while the air quality is much better in summer. Then, the data of (a) Landsat 8

OLI remote sensing images at UTC 2:54 (viz. 10:54 am Beijing time), on 30 December 2016 (winter) (see Figure 10, below) and UTC 2:54, on 24 August 2016 (summer) (see Figure 11, below) in Beijing and (b) NOAA meteorological data for the same region and at the approximate time points, are selected and retained. All the other data in December and August of 2016 were removed from the BR-PM_x models.

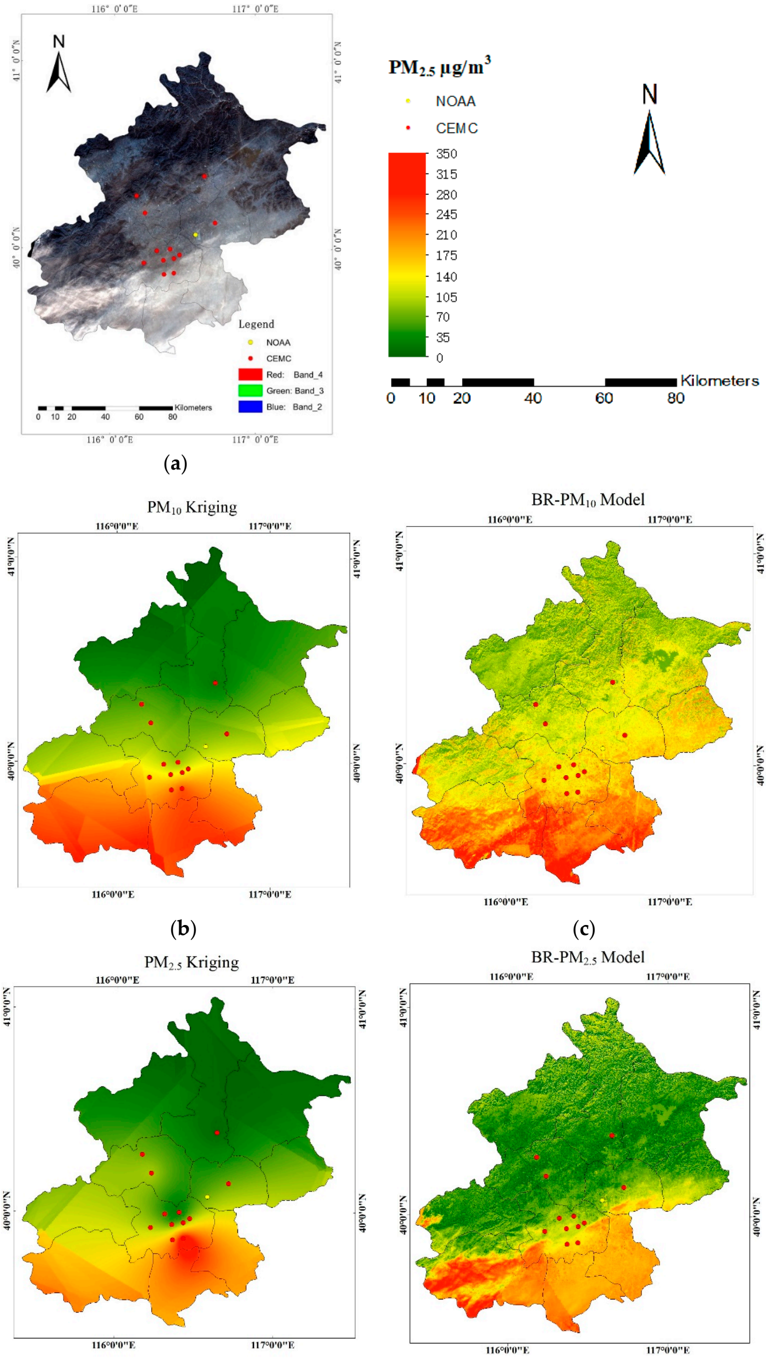

(a)

PM_{10} Kriging

BR-PM_{10} Model

(b) (c)

$PM_{2.5}$ Kriging

BR-$PM_{2.5}$ Model

(d) (e)

Figure 10. Spatial distributions of the PM_{10} and $PM_{2.5}$ concentrations (μg/m^3) over the Beijing area at UTC 2:54 on 30 December 2016: (**a**) the Landsat 8 OLI image of RGB true color; (**b**) the PM_{10} concentration calculated by the method of Kriging interpolation; (**c**) the results estimated by the BR-PM_{10} model; (**d**) the $PM_{2.5}$ concentration calculated by the method of Kriging interpolation; and (**e**) the results estimated by the BR-$PM_{2.5}$ model.

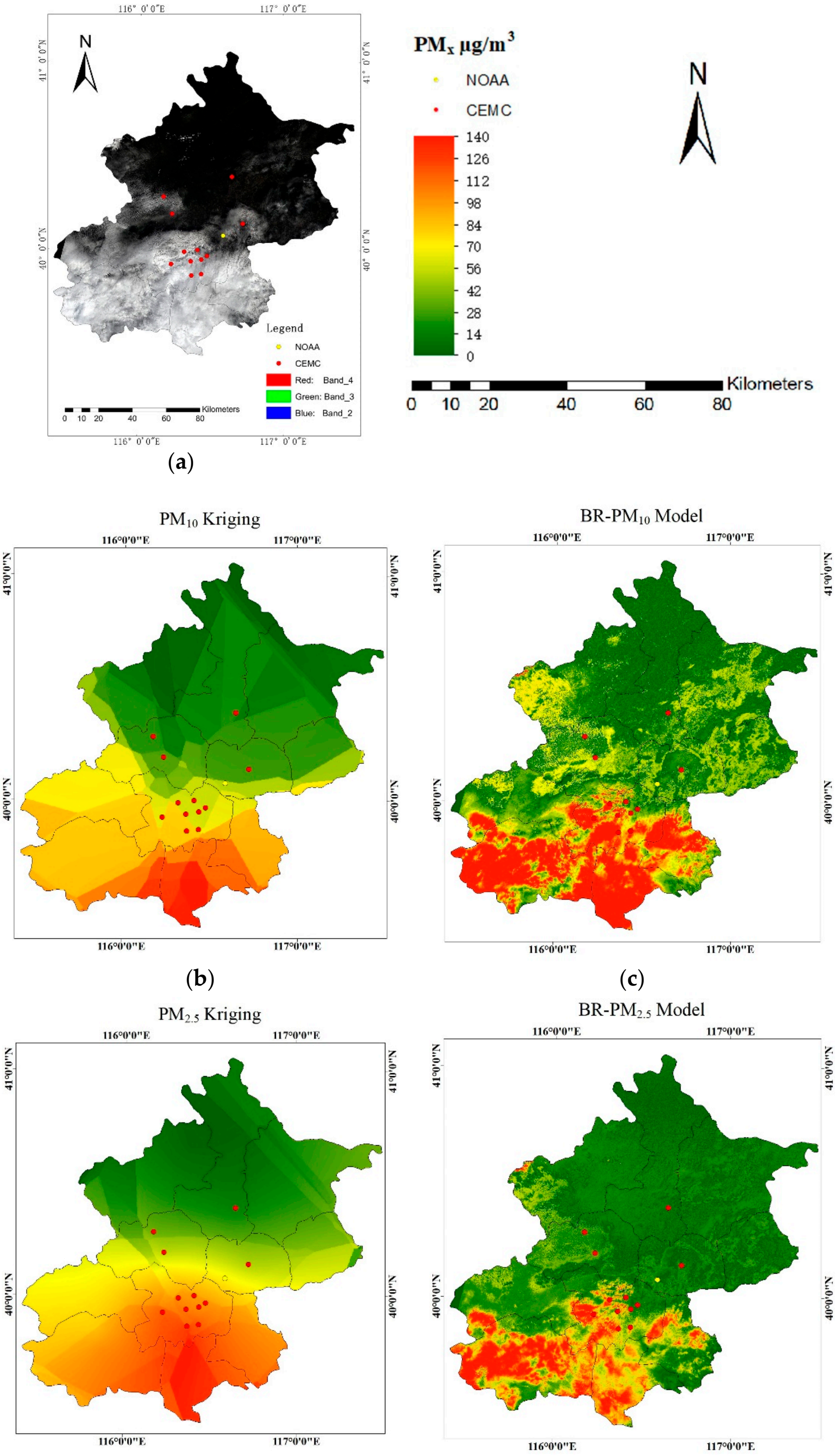

(**a**)

(**b**) (**c**)

(**d**) (**e**)

Figure 11. Spatial distributions of the PM_{10} and $PM_{2.5}$ concentrations (μg/m^3) over the Beijing area at UTC 2:54 on 24 August 2016: (**a**) the Landsat 8 OLI image of RGB true color; (**b**) the PM_{10} concentration calculated by the method of Kriging interpolation; (**c**) the results estimated by the BR-PM_{10} model; (**d**) the $PM_{2.5}$ concentration calculated by the method of Kriging interpolation; and (**e**) the results estimated by the BR-$PM_{2.5}$ model.

To obtain the continuous distribution graph of the PM_x concentrations of the research area, one of the common methods is to operate the spatial interpolation based on the discrete PM_x values at various points. Figure 10b,d and Figure 11b,d are such spatial distribution graphs calculated by the Kriging interpolations based on the monitoring PM_x values from the 12 CEMC stations located in the area of Beijing, China. Figure 10c,e and Figure 11c,e are the spatial distribution graphs of the PM_{10} and $PM_{2.5}$ concentrations estimated by the proposed BR-PM_x models in this research. All of these graphs have the spatial resolution of 30 m.

The estimation results of the BR-PM_x models and the interpolation results are consistent with respect to the spatial distribution. The higher PM_x values are distributed in the south, while the lower values are located in the north, which are not only related to the special terrain of Beijing but also to the industrialization and population density. Furthermore, the minimum (Min), maximum (Max) and the mean values of the PM_x concentrations, which are respectively generated by Kriging interpolations and the BR-PM_x models, have been illustrated as well as compared in Tables 3 and 4 (below). Tables 3 and 4 demonstrate that, under both of the conditions with (a) heavy air pollution at UTC 2:54 on 30 December 2016 and (b) mild air pollution at UTC 2:54 on 24 August 2016, the coefficient of determination (R^2) between Kriging interpolation and BR-$PM_{2.5}$ model reached 0.80817 and 0.82954 respectively, while the R^2 of PM_{10} are respectively 0.77442 and 0.75519: the distribution trend of the PM_x concentrations graph generated by Kriging interpolation and BR-PM_x models remained consistent regardless of whether the air is heavily polluted or not.

Table 3. Comparison of the PM_x-concentration distributions generated by Kriging interpolation and the BR-PM_x models at UTC 2:54 on 30 December 2016 (in winter).

Category	Min (μg/m^3)	Max (μg/m^3)	Mean (μg/m^3)	R^2 between (a) and (b)
(a) $PM_{2.5}$ Kriging interpolation	46.43	316.41	127.97	0.80817
(b) Estimation by BR-$PM_{2.5}$ Model	24.92	336.42	145.88	
(a) PM_{10} Kriging interpolation	105.67	271.91	174.11	0.77442
(b) Estimation by BR-PM_{10} Model	71.45	323.52	169.46	

Table 4. Comparison of the PM_x-concentration distributions generated by Kriging interpolation and the BR-PM_x models at UTC 2:54 on 24 August 2016 (in summer).

Category	Min (μg/m^3)	Max (μg/m^3)	Mean (μg/m^3)	R^2 between (a) and (b)
(a) $PM_{2.5}$ Kriging interpolation	33.76	65.19	47.54	0.82954
(b) Estimation by BR-$PM_{2.5}$ Model	14.26	87.31	38.65	
(a) PM_{10} Kriging interpolation	51.66	101.87	69.22	0.75519
(b) Estimation by BR-PM_{10} Model	23.12	125.38	53.74	

After the validation analysis, it can be concluded that the proposed BR-PM_x models are feasible for the PM_x concentration estimations with the air pollution in different degrees, and thereby have a certain potential for real-world applications.

4. Discussion

Taking advantage of the wide spatial and temporal coverage, it has been generally proved that the various satellite remote sensing images could be employed for the estimation of the PM_x concentrations in large geographic areas. In order to obtain the continuous spatial distribution of PM_x concentrations in various cities of China, this research develops new BR-PM_x models for the estimation of PM_x (including PM_{10} and $PM_{2.5}$) concentrations based on the algorithm of a multilayer perceptron neural network combined with LLZ method. In the BR-PM_x models, the primary source data were from Landsat 8 OLI and in the meantime, various meteorological factors and the time parameter have been taken into consideration. To the best of our knowledge, the Landsat 8 OLI satellite data have been seldom investigated for the PM_x concentration estimations in the literature published so far.

With an explore process with stepwise enlarged areas, the optimal LLZ for Beijing has been identified. Then, the coefficient of determination (R^2) of the BR-$PM_{2.5}$ and BR-PM_{10} models respectively reached 0.795 and 0.773; synchronously, the RMSE values of the BR-$PM_{2.5}$ and BR-PM_{10} models reduced to 31.27 $\mu g/m^3$ and 20.09 $\mu g/m^3$, respectively. The estimation accuracy is satisfactory and higher than many established models based on the AOD method [19,20,24,49]. To make the validation analysis, the BR-PM_x models have been implemented to obtain the spatial distribution graph of the PM_x concentrations in Beijing at two different times: one is in winter with heavily polluted air and the other is in summer with much better air quality. The distribution graphs generated by the BR-PM_x models are significantly better than that of Kriging interpolations in terms of resolution and clarity.

Furthermore, as the Landsat 8 OLI remote sensing images have been employed as the primary source data in this research, the distribution graphs of PM_x concentrations estimated by the PM_x models have a much higher spatial resolution than many other research works, e.g., the estimated PM_x concentrations calculated by the AOD method in [19–21,24,50], which is based on the MODIS data with the highest resolution of 250 m.

Therefore, the proposed BR-PM_x models can be used as one of the possible methods to estimate the general spatial distributions of PM_x concentrations in various cities in China that have been monitored by CEMC stations.

5. Conclusions

In this research, we developed a new BR-PM_x model to estimate the PM_x concentration, which is based on the spectral data of Landsat 8 OLI remote sensing images and the PM_x concentration data from the ground monitoring stations. During the process of analyzing the correlations between PM_{est} and PM_{rea} in terms of temporal dimensions with the data from May 2014 to May 2018, satisfactory estimation results cannot be obtained if the whole area of China is set as an estimation region and the regression coefficient R^2 between PM_{est} and PM_{rea} for the models BR-$PM_{2.5}$ and BR-PM_{10} just reach ca. 0.3647 and 0.2928, respectively. The estimation results represent typical characteristics of seasonal variations. The period with the highest estimation accuracy is in autumn for both the BR-$PM_{2.5}$ and BR-PM_{10} models.

To improve the estimation performance of the BR-PM_x model, the factor of latitude and longitude zone (LLZ) has been integrated into the model to obtain the optimal training area for the specific research area of Beijing, China. The results demonstrate that the LLZ method performs promisingly as the coefficient of determination (R^2) of the BR-$PM_{2.5}$ and BR-PM_{10} models reached 0.795 and 0.773, respectively; their RMSE reached 31.27 $\mu g/m^3$ for the BR-$PM_{2.5}$ model and 20.09 $\mu g/m^3$ for the BR-PM_{10} model.

In general, based on the Landsat 8 OLI remote sensing images and the PM_x concentration data, the MLP neural network combined with the LLZ method produced reasonable estimation results of PM_x concentration in the test area of Beijing, China. As known, there are some deficiencies in the LLZ method due to the nonuniform distribution of the observation stations. In addition, it is difficult to determine the optimal bandwidth accurately since the optimal bandwidth can vary from one area to another. Due to the fact that the regional characteristics of aerosols can be taken into account by the LLZ method, the LLZ method is very useful to solve the problems of missing or having few observation stations in the research area by acquiring the training data from the surrounding stations. The BR-PM_x models after the training in the optimal LLZs can then be utilized to analyze the air pollution characteristics of the investigated research areas. Meanwhile, the high-resolution (30 m) estimations of PM_x concentrations with complete spatial coverage were derived in this research. From the perspective of daily coverage, the estimation results are quite close to the observation values. Hence, the estimation results can help to (a) understand the formation process of regional PM_x

pollution episodes, (b) obtain accurate PM_x sources and distributions with high spatial resolution and (c) establish pollution control measures.

In this research, the meteorological factors of RH, TEMP, WD, WS and PRS were considered in the developed BR-PM_x models. In our future work, some other parameters (e.g., the planetary boundary layer) and the sensitivity analysis of the employed parameters will be further investigated. Moreover, it should make some sense if the AOD method and the proposed BR-PM_x models can be integrated together.

Author Contributions: B.Z., M.Z. and X.Z. conceived and designed the study; B.Z. and J.K. collected and analyzed the data; B.Z. completed the experiments and software; M.Z. and X.Z. initiated the overall research question and M.Z. found funding for this project; B.Z. and M.Z. drafted the paper; D.H. and J.X. critically read and revised the draft. All authors read and approved the final manuscript.

Funding: This research was funded by (a) the National Natural Science Foundation of China, Grant No. 41871315, and (b) the European Research Council (ERC) under the European Union's Horizon 2020 research and innovation program, Grant No.ERC-2016-StG-714087.

Acknowledgments: This research is supported by (a) the Helmholtz Association under the framework of the Young Investigators Group "SiPEO" (VH-NG-1018, www.sipeo.bgu.tum.de), (b) the Bavarian Academy of Sciences and Humanities in the framework of Junges Kolleg, and (c) the Data Center for Resources and Environmental Sciences, Chinese Academy of Sciences (RESDC) (http://www.resdc.cn) as the data provider.

Conflicts of Interest: The authors declare no conflict of interest.

References

1. Geng, G.; Zhang, Q.; Martin, R.V.; Donkelaar, A.V.; Huo, H.; Che, H.; Lin, J.; He, K. Estimating long-term PM 2.5 concentrations in China using satellite-based aerosol optical depth and a chemical transport model. *Remote Sens. Environ.* **2015**, *166*, 262–270. [CrossRef]
2. King, M.D.; Kaufman, Y.J.; Menzel, W.P.; Tanré, D. Remote sensing of cloud, aerosol, and water vapor properties from the moderate resolution imaging spectrometer (MODIS). *IEEE Trans. Geosci. Remote Sens.* **1992**, *30*, 2–27. [CrossRef]
3. Peng, J.; Chen, S.; Lü, H.; Liu, Y.; Wu, J. Spatiotemporal patterns of remotely sensed PM 2.5 concentration in China from 1999 to 2011. *Remote Sens. Environ.* **1999**, *174*, 109–121. [CrossRef]
4. Gauderman, W.J.; Avol, E.; Gilliland, F.; Vora, H.; Thomas, D.; Berhane, K.; McConnell, R.; Kuenzli, N.; Lurmann, F.; Rappaport, E.; et al. The effect of air pollution on lung development from 10 to 18 years of age. *N. Engl. J. Med.* **2004**, *351*, 1057–1067. [CrossRef] [PubMed]
5. Hoek, G.; Krishnan, R.M.; Beelen, R.; Peters, A.; Ostro, B.; Brunekreef, B.; Kaufman, J.D. Long-term air pollution exposure and cardio-respiratory mortality. *Environ. Health* **2013**, 12–43. [CrossRef]
6. Pascal, M.; Falq, G.; Wagner, V.; Chatignoux, E.; Corso, M.; Blanchard, M.; Host, S.; Pascal, L.; Larrieu, S. Short-term impacts of particulate matter (PM 10, PM 10–2.5, PM 2.5) on mortality in nine French cities. *Atmos. Environ.* **2014**, *95*, 175–184. [CrossRef]
7. Pope, C.A.; Burnett, R.T.; Thun, M.J.; Calle, E.E.; Krewski, D.; Ito, K.; Thurston, G.D. Lung cancer, cardiopulmonary mortality, and long-term exposure to fine particulate air pollution. *J. Am. Med. Assoc.* **2002**, *287*, 1132–1141. [CrossRef]
8. You, W.; Zang, Z.; Zhang, L.; Li, Z.; Chen, D.; Zhang, G. Estimating ground-level PM10 concentration in northwestern China using geographically weighted regression based on satellite AOD combined with CALIPSO and MODIS fire count. *Remote Sens. Environ.* **2015**, *168*, 276–285. [CrossRef]
9. Christodoulakis, J.; Varotsos, C.A.; Cracknell, A.P.; Kouremadas, G.A. The deterioration of materials as a result of air pollution as derived from satellite and ground based observations. *Atmos. Environ.* **2018**, *185*, 91–99. [CrossRef]
10. Ma, Z.; Hu, X.; Huang, L.; Bi, J.; Liu, Y. Estimating ground-level PM2.5 in China using satellite remote sensing. *Environ. Sci. Technol.* **2014**, *48*, 7436. [CrossRef]
11. Zou, B.; Pu, Q.; Bilal, M.; Weng, Q.; Zhai, L.; Nichol, J.E. High-Resolution Satellite Mapping of Fine Particulates Based on Geographically Weighted Regression. *IEEE Geosci. Remote Sens. Lett.* **2017**, *13*, 495–499. [CrossRef]

12. Zou, B.; Zheng, Z.; Wan, N.; Qiu, Y.; Wilson, J.G. An optimized spatial proximity model for fine particulate matter air pollution exposure assessment in areas of sparse monitoring. *Int. J. Geogr. Inf. Sci.* **2016**, *30*, 727–747. [CrossRef]
13. Mukai, S.; Sano, I.; Takashima, T.; Yamaguchi, Y. Aerosol retrieval based on photopolarimetry. In Proceedings of the International Geoscience and Remote Sensing Symposium (IGARSS), Pasadena, CA, USA, 8–12 August 1994; Volume 4, pp. 1898–1900.
14. Afonin, S.V. An appraisal of the method of AOD retrieval over land according to MODIS satellite measurements in IR spectral range. *Atmos. Ocean. Opt.* **2011**, *24*, 584–586. [CrossRef]
15. Moon, T.; Wang, Y.; Liu, Y.; Yu, B. Evaluation of a MISR-based high-resolution aerosol retrieval method using AERONET DRAGON campaign data. *IEEE Trans. Geosci. Remote Sens.* **2015**, *53*, 4328–4339. [CrossRef]
16. Zhang, J.; Si, Z.; Mao, J.; Wang, M. Remote Sensing Aerosol Optical Depth over China with GMS-5 Satellite. *Chin. J. Atmos. Sci.* **2003**, *27*, 23–35. [CrossRef]
17. He, J.; Zha, Y.; Zhang, J.; Gao, J.; Li, Y.; Chen, X. Retrieval of aerosol optical thickness from HJ-1 CCD data based on MODIS-derived surface reflectance. *Int. J. Remote Sens.* **2015**, *36*, 882–898. [CrossRef]
18. Ge, B.; Yang, L.; Chen, X.; Li, Z.I.; Mei, X.; Liu, L. Study on aerosol optical depth retrieval over land from Himawari-8 data based on dark target method. *J. Remote Sens.* **2018**, 38–50. [CrossRef]
19. Li, R.; Sun, L. An Improved DDV Method to Retrieve Aerosol Optical Depth for Landsat 8 OLI Image. *Remote Sens. Inf.* **2017**, *32*, 120–125. [CrossRef]
20. Koelemeijer, R.; Homan, C.D.; Matthijsen, J. Comparison of spatial and temporal variations of aerosol optical thickness and particulate matter over Europe. *Atmos. Environ.* **2006**, *40*, 5304–5315. [CrossRef]
21. Liu, Y.; Franklin, M.; Kahn, R.; Koutrakis, P. Using aerosol optical thickness to predict ground-level PM 2.5 concentrations in the St. Louis area: A comparison between MISR and MODIS. *Remote Sens. Environ.* **2007**, *107*, 33–44. [CrossRef]
22. Nicolantinio, W.D.; Cacciari, A.; Bolzacchini, V.; Ferrero, V.; Volta, M.; Pisoni, E. MODIS aerosol optical properties over North Italy for estimating surface-level $PM_{2.5}$. In Proceedings of the Envisat Symposium 2007, Montreux, Switzerland, 23–27 April 2007.
23. Gupta, P.; Christopher, S.A. Particulate matter air quality assessment using integrated surface, satellite, and meteorological products: Multiple regression approach. *J. Geophys. Res.* **2009**, D14205. [CrossRef]
24. Gupta, P.; Christopher, S.A.; Wang, J.; Gehrig, R.; Lee, Y.; Kumar, N. Satellite remote sensing of particulate matter and air quality assessment over global cities. *Atmos. Environ.* **2006**, *40*, 5880–5892. [CrossRef]
25. Liu, Y.; Sarnat, J.A.; Kilaru, V.; Jacob, D.J.; Koutrakis, P. Estimating ground-level $PM_{2.5}$ in the eastern United States using satellite remote sensing. *Environ. Sci. Technol.* **2005**, *39*, 3269–3278. [CrossRef] [PubMed]
26. Hong, D.; Yokoya, N.; Xu, J.; Zhu, X. Joint & progressive learning from high-dimensional data for multi-label classification. In Proceedings of the European Conference on Computer Vision (ECCV), Munich, Germany, 8–14 September 2018; pp. 469–484.
27. Xu, J.; Schüssler, O.; Rodriguez, D.G.L.; Romahn, F.; Doicu, A. A Novel Ozone Profile Shape Retrieval Using Full-Physics Inverse Learning Machine (FP-ILM). *IEEE J. Sel. Top. Appl. Earth Obs. Remote Sens.* **2017**, *10*, 5442–5457. [CrossRef]
28. Paciorek, C.J.; Liu, Y. Limitations of Remotely Sensed Aerosol as a Spatial Proxy for Fine Particulate Matter. *Environ. Health Perspect.* **2009**, *117*, 904–909. [CrossRef] [PubMed]
29. Kumar, N. What Can Affect AOD–$PM_{2.5}$ Association. *Environ. Health Perspect.* **2010**, *118*, A109–A110. [CrossRef] [PubMed]
30. Guo, G.; Ma, L. Urban aerosol optical thickness retrieval from MODIS data. *Remote Sens. Technol. Appl.* **2005**, *20*, 343–345. [CrossRef]
31. Dong, J.; Xiao, X.; Menarguez, M.A.; Zhang, G.; Qin, Y.; Thau, D.; Biradar, C.; Moore, B. Mapping paddy rice planting area in northeastern Asia with Landsat 8 images, phenology-based algorithm and Google Earth Engine. *Remote Sens. Environ.* **2016**, *185*, 142–154. [CrossRef]
32. Krishnan, S.P.T.; Gonzalez, J.L. *Building Your Next Big Thing with Google Cloud Platform*; A Press: Berkeley, CA, USA, 2015; pp. 28–49. ISBN 978-1-4842-1004-8.
33. Patel, N.N.; Angiuli, E.; Gamba, P.; Gaughan, A.; Lisini, G.; Stevens, F.R.; Tatem, A.J.; Trianni, G. Multitemporal settlement and population mapping from Landsat using Google Earth Engine. *Int. J. Appl. Earth Obs.* **2015**, *35*, 199–208. [CrossRef]

34. Rivas, I.; Mazaheri, M.; Viana, M.; Moreno, T.; Cifford, S.; He, C.; Bischof, O.F.; Martins, V.; Reche, C.; Alastuey, A.; et al. Identification of technical problems affecting performance of DustTrak DRX aerosol monitors. *Sci. Total Environ.* **2017**, *584–585*, 849–855. [CrossRef] [PubMed]
35. Ghanem, D.; Zhang, J. Effortless Perfection: Do Chinese Cities Manipulate 'Blue Skies?'. *SSRN Electron. J.* **2013**, *68*, 203–225. [CrossRef]
36. Tian, J.; Chen, D. A semi-empirical model for predicting hourly ground-level fine particulate matter ($PM_{2.5}$) concentration in southern Ontario from satellite remote sensing and ground-based meteorological measurements. *Remote Sens. Environ.* **2010**, *114*, 221–229. [CrossRef]
37. Zhu, X.X.; Tuia, D.; Mou, L.; Xia, G.S.; Zhang, L.; Xu, F.; Fraundorfer, F. Deep Learning in Remote Sensing: A Comprehensive Review and List of Resources. *IEEE Geosci. Remote Sens. Mag.* **2017**, *5*, 8–36. [CrossRef]
38. Hong, D.; Liu, W.; Su, J.; Pan, Z.; Wang, G. A novel hierarchical approach for multispectral palmprint recognition. *Neurocomputing* **2015**, *151*, 511–521. [CrossRef]
39. Lee, S.; Choeh, J.Y. Predicting the helpfulness of online reviews using multilayer perceptron neural networks. *Expert Syst. Appl.* **2014**, *41*, 3041–3046. [CrossRef]
40. Zhu, Q.; Cai, Y.; Liu, L. A global learning algorithm for a RBF network. *Neural Netw.* **1999**, *12*, 527–540. [CrossRef]
41. Farhat, N.H.; Psaltis, D.; Prata, A.; Paek, E. Optical Implementation of The Hopfield Model. *Appl. Opt.* **1985**, *24*, 1469. [CrossRef] [PubMed]
42. Ramadhas, A.S.; Jayaraj, S.; Muraleedharan, C.; Padmakumari, K. Artificial neural networks used for the prediction of the cetane number of biodiesel. *Renew. Energy* **2006**, *31*, 2524–2533. [CrossRef]
43. Meng, X.; Jia, M.; Wang, T. Neural network prediction of biodiesel kinematic viscosity at 313 K. *Fuel* **2014**, *121*, 133–140. [CrossRef]
44. Rashidi, A.M.; Hayati, M.; Rezaei, A. Prediction of the relative texture coefficient of nanocrystalline nickel coatings using artificial neural networks. *Solid State Sci.* **2011**, *13*, 1589–1593. [CrossRef]
45. Gardner, M.W.; Dorling, S.R. Artificial neural networks (the multilayer perceptron)—A review of applications in the atmospheric sciences. *Atmos. Environ.* **1998**, *32*, 2627–2636. [CrossRef]
46. Liu, J.; Li, J.; Li, W. Temporal Patterns in Fine Particulate Matter Time Series in Beijing. *Sci. Rep.* **2016**, *6*, 32221. [CrossRef] [PubMed]
47. Ming, L.; Jin, L.; Li, J.; Fu, P.; Yang, W.; Liu, D.; Zhang, G.; Wang, Z.; Li, X. PM2.5 in the Yangtze River Delta, China: Chemical compositions, seasonal variations, and regional pollution events. *Environ. Pollut.* **2017**, *223*, 200–212. [CrossRef]
48. Engel-Cox, J.A.; Holloman, C.H.; Coutant, B.W.; Hoff, R.M. Qualitative and quantitative evaluation of MODIS satellite sensor data for regional and urban scale air quality. *Atmos. Environ.* **2004**, *38*, 2495–2509. [CrossRef]
49. Just, A.C.; Wright, R.O.; Schwartz, J.; Coull, B.A.; Baccarelli, A.A.; Tellez-Rojo, M.M.; Moody, E.; Wang, Y.; Lyapustin, A.; Kloog, I. Using high-resolution aerosol optical depth to estimate daily $PM_{2.5}$ geographical distribution in Mexico City. *Environ. Sci. Technol.* **2015**, *49*, 8576–8584. [CrossRef]
50. Ma, Z.; Hu, X.; Sayer, A.M.; Levy, R.; Zhang, Q.; Xue, Y.; Tong, S.; Bi, J.; Huang, L.; Liu, Y. Satellite-Based Spatiotemporal Trends in $PM_{2.5}$ Concentrations: China, 2004–2013. *Environ. Health Perspect.* **2016**, *124*, 184–192. [CrossRef] [PubMed]